Front. Chem. Sci. Eng. 2025, 19(5): 38
https://doi.org/10.1007/s11705-025-2539-0

RESEARCH ARTICLE

Stable lithium metal batteries enabled by Al-Li/LiF composite artificial interfacial layer

Guojie Li[1,2], Xuan Liang[1], Junlong Zhang[1], Bin Guo[1], Baoguang Mao[4], Hongming Sun[5], Aoxuan Wang (✉)[2], Qibo Deng (✉)[3], Chuntai Liu[1]

1 State Key Laboratory of Structural Analysis, Optimization and CAE Software for Industrial Equipment, National Engineering Research Center for Advanced Polymer Processing Technology, Zhengzhou University, Zhengzhou 450002, China
2 Key Laboratory for Green Chemical Technology of Ministry of Education, School of Chemical Engineering and Technology, Tianjin University, Tianjin 300072, China
3 School of Mechanical Engineering, Hebei University of Technology, Tianjin 300401, China
4 State Key Laboratory of Organic-Inorganic Composites, College of Chemical Engineering, Beijing University of Chemical Technology, Beijing 100029, China
5 Tianjin Key Laboratory of Structure and Performance for Functional Molecules, College of Chemistry, Tianjin Normal University, Tianjin 300387, China

Abstract Lithium metal anode represents the ultimate solution for next-generation high-energy-density batteries but is plagued from commercialization by side reactions, substantial volume fluctuation, and the notorious growth of lithium dendrites. These hazardous issues are further aggravated under real-world conditions. In this study, a stable Al-Li/LiF artificial interphase with rapid ion transport pathways is created through a one-step chemical pretreatment process, effectively addressing these challenges simultaneously. As a consequence, the composite interfacial layer exhibits exceptional ionic conductivity, mechanical strength, and electrolyte wettability, ensuring swift Li^+ transfer diffusion while suppressing lithium dendrite growth. Remarkably, the Al-Li/LiF symmetric cell provides a cycle life exceeding 2300 h with a low polarization at 0.5 $mA \cdot cm^{-2}$. Furthermore, its enhanced cycling stability and capacity retention as well as capacity utilization stability pairing with $LiFePO_4$ and $LiNi_{0.8}Co_{0.1}Mn_{0.1}O_2$ cathodes, highlighting the proposed approach as a promising solution for practical Li metal batteries.

Keywords lithium metal anode, artificial solid electrolyte interphase, dendrite growth, stability

Received November 29, 2024; accepted January 21, 2025;
online March 25, 2025

E-mails: aoxuanwang@tju.edu.cn (Wang A.),
qibodeng@hebut.edu.cn (Deng Q.)

1 Introduction

Lithium metal stands out as the most promising anode material due to its exceptionally low redox potential (–3.04 V vs. standard hydrogen electrode) and the remarkable theoretical capacity (3860 $mAh \cdot g^{-1}$) [1–5]. Nevertheless, unlimited volume expansion, and the fragility of the solid-electrolyte-interphase (SEI) often lead to the formation of lithium dendrites and inactive "dead lithium" [6–9]. This irreversible process consumes both lithium and electrolytes, resulting in persistent capacity degradation and low Coulombic efficiency (CE). Furthermore, lithium dendrites and dead lithium also pose significant safety risks for Li metal batteries (LMBs) [10–14]. Thus, stabilizing Li metal anode (LMA) is critical to achieving viable LMBs [15–19].

Various approaches have been explored to stabilize the electrode/electrolyte interface employing techniques such as electrolyte additives, localized high-concentration electrolyte and artificial protective layers [20–23]. Although significant progress have been made in understanding and designing the electrode/electrolyte interface, *in situ* SEI generated via electrolyte alteration is challenging to maintain during long-term deposition-dissolution. The application of artificial SEI on the surface of LMA is thought to be an effective strategy for protecting the Li metal. The artificial layer avoids direct contact between Li metal and liquid electrolyte, thereby slowing their consumption, and inhibiting heterogeneous deposition and dendrite formation, which is to regulate Li metal deposition behavior by artificially constructing a

stable protective layer on the LMA prior to the cell cycle, as well as precisely managing the electrolyte-LMA interface composition and properties. An ideal SEI should have the following characteristics: (1) high chemical and electrochemical stability to prevent side reactions; (2) excellent electronic insulation to avoid side reactions between the electrolyte and LMA; (3) high ionic conductivity to facilitate Li^+ diffusion, while prohibiting electrons and solvent molecules from passing through; (4) high mechanical strength to resist breakage.

Recently, the fluorination of Li metal surface to obtain LiF as the principle component of SEI has been widely adopted to improve the cyclic stability of LMA [24,25]. LiF is a superlative electronic insulator, possessing a wide band gap that effectively resists electron tunneling [26]. When LiF is integrated with other components at nanoscale, the resulting interphase exhibits high ionic conductivity, low diffusion energy, and high surface energy, resulting in both rapid Li^+ kinetics and parallel rather than vertical lithium electrodeposition [27]. Consequently, the LiF-based interfacial layer ensure an improved surface topography of lithium deposits and serves as a strong barrier to lithium dendrite growth [28]. In addition to LiF, lithium-based alloy that acts as a protective interface to inhibit dendrite growth has been investigated. Such alloy methods include lithium tin, lithium magnesium, lithium bismuth, etc [29]. The alloy phase efficiently reduces the diffusion barrier of Li^+ and improves the stability of the Li metal interface.

Taking these considerations into account, a composite artificial interphase enriched with LiF and aluminum lithium (Al-Li) alloy is crafted by altering the LMA with AlF_3. In addition to eliminating dead lithium and lithium dendrites, artificially generated LiF and Al-Li alloy artificial SEI can deposit lithium in the lower section of the modified interface by promoting ion transport. Hybrid lithium symmetric batteries exhibit a significantly longer and more stable deposition/dissolution cycle (more than 2300 h) as compared to pure Li cells. Li metal cells outperform pure Li cells in terms of cycle stability, rate performance, and capacity retention when matched with LFP and NCM811 cathode. The design of the artificial SEI provides a new solution to the challenge of LMA.

2 Experimental

2.1 Materials

AlF_3, dimethyl ether (DME) and fluoroethylene carbonate (FEC) were purchased from Shanghai Aladdin Biochemical Technology Co., Ltd., China, Lithium iron phosphate (LFP), $LiNi_{0.8}Co_{0.1}Mn_{0.1}O_2$ (NCM811), *N*-methyl-2-pyrrolidone (NMP) and polyvinylidene fluoride (PVDF) were obtained from Shenzhen Kejing Zhida Technology Co., Ltd., China. 1 mol·L^{-1} $LiPF_6$-ethylene carbonate/diethyl carbonate (EC/DEC) (1:1, v/v) is provided by Suzhou Fosai New Material Co., Ltd.

2.2 Fabrication of Al-Li/LiF anode

First, AlF_3 powders of varying qualities are added to a specific amount of DME solvent, magnetically stirred at room temperature for 30 min, and then placed in the ultrasonic cleaning machine for 30 min, so that the AlF_3 powders are evenly dispersed in the solvent. Subsequently, the AlF_3 dispersions of different concentrations are repeatedly applied onto the Li metal and placed in the muffle furnace to promote the reaction between Li metal and AlF_3, and then an artificial protective layer containing LiF and Al-Li alloy is generated on the surface of the LMA. Finally, washing with solvents removes excess salt from the surface. All these operations are carried out in an argon glove box (H_2O < 0.1 ppm, O_2 < 0.1 ppm).

2.3 Characterizations

The morphologies of LMA before and after cycling are systematically characterized using scanning electron microscopy (SEM, Hitachi) coupled with energy-dispersive X-ray analysis (Oxford Instruments). X-ray photoelectron spectroscopy (XPS) measurements are performed on a PHI-5000 Versaprobe XPS spectrometer. Phase analysis of lithium surface is measured by the X-ray diffraction (XRD, Bruker, Cu Kα, λ = 0.15418 nm). Atomic force microscopy (AFM, Bruker Dimensionicon) is used to obtain the Young's modulus of Li metal surface. The contact angle is measured by a Kruss DSA100 (Dataphysics Corp. Germany), and a 5 μL droplet of ester electrolyte utilized the experiment.

2.4 Electrochemical measurement

CR2032-type coin cells, equipped with a microporous polypropylene separator (Celgard 2400), are assembled within the aforementioned argon-filled glove box. The electrochemical performance of all cells evaluated using the LAND battery test system. Electrochemical impedance spectrum (EIS) and linear sweep voltammetry (LSV) measurements are performed by an electrochemical workstation (CHI660E), and LSV is tested in the range from –0.1 to 0.1 V at a scan rate of 1 mV·s^{-1}.

The symmetric cells employ 60 μL of an ester electrolyte, consisting of 1 mol·L^{-1} $LiPF_6$ dissolved in an EC/DEC solvent (volume ratio 1:1), and constant current charge/discharge tests are performed using different current densities. To obtain LFP/NCM811 cathode, first, LFP/NCM811 powder, Super P, and PVDF (mass ratio of 7:2:1) are mixed with NMP as a solvent to prepare a slurry and coated it onto clean aluminum foil. Then, the

LFP/NCM811 cathode with a diameter of 12 mm is obtained by slicing after evaporating the solvent under vacuum at 120 °C for 4 h. In the experiment, FEC is utilized as an electrolyte additives to form a protective film on the surface of the cathode to prevent further decomposition of the main components of the electrolyte for the assembly of high voltage Li||NCM811 full cells [19]. 70 μL 1 mol·L^{-1} $LiPF_6$ dissolved in EC/DEC (volume ratio of 1:1) solvent mixture with 10 wt % FEC is used as the electrolyte of the full cells.

3 Results and discussion

A diagram depicting the growth of Li dendrites on bare Li metal and the formation of dead lithium during the deposition/dissolution process (Fig. 1(a)). Figure 1(b) features a uniform protective layer formed on the surface of the lithium electrode upon treatment with AlF_3, accompanied by a schematic diagram that highlights its capacity to ensure consistent plating/stripping throughout the cycling procedures.

To optimize the thickness of the SEI protective layer, dispersions containing 0.5, 1.5 and 2.5 wt % AlF_3 dissolved in DME are adopted, abbreviated as 0.5-AF, 1.5-AF and 2.5-AF, respectively. Optical and SEM images are used to charactorize the artificial SEI layer, as presented in Fig. 2. The surface of pure Li metal shows a silver luster (Fig. 2(a)), which gradually transitions to gray following treatment. As can be seen from Fig. 2(b), the artificial SEI layer derived from with 0.5-AlF does not fully cover and protect the lithium surface completely from reacting with the electrolyte, leading to low CE and capacity decay. For comparison, complete coverage of the artificial SEI layer may be obtained with 1.5-AF and 2.5-AF treatments (Figs. 2(c) and 2(d)), showing no pinholes or cracks. Cross-section SEM images (Figs. 2(e–h)) reveal that the average thickness of artificial SEI treated with 0.5-AF, 1.5-AF and 2.5-AF is 10, 20, and 40 μm, respectively. A thicker SEI layer result in slower Li^+ diffusion kenetics and higher impedance due to the increased Li^+ transport distance. As a result, it is necessary to optimize the thickness of the SEI layer, in order to protect the metal lithium anode from side reactions with the electrolyte while simultaneously providing excellent Li^+ conductivity.

Lithium electrodes protected by 10, 20, and 40 μm thick artificial SEI layer are abbreviated as LAF-10, LAF-20, and LAF-40, respectively. Figure 2(i) presents the galvanostatic Li plating/stripping profiles of treated Li sheets and pure Li sheets at current density of 0.5 mA·cm^{-2} with capacity of 1 mAh·cm^{-2}. The pure Li anode exhibits stable cycling for only 600 h, with a higher overpotential that progressively increases over time. LAF-10, LAF-20 and LAF-40 electrodes can stabilize the cycle for more than 800, 2000 and 1600 h, respectively. In summary, LAF-20 has the lowest overpotential and the longest cycle life.

To further explore the optimal thickness of the SEI protective layer, the SEI layer treated with different concentrations of AlF_3 is characterized. The charge transfer resistance (R_{ct}) of a symmetric cell is calculated by impedance measurement. Figure 2(g) illustrates the EIS spectra of pure Li, LAF-10, LAF-20 and LAF-40 respectively. The impedance results are fitted by an equivalent circuit (Fig. S1, cf. Electronic Supplementary Material, ESM). There is no obvious protective film on pure Li before the electrochemical cycling due to the primary SEI exists when pure Li by reacting with the electrolyte is very thin and uneven. The side reaction can lead to significant interface resistance. The R_s of the AlF_3-treated lithium electrode symmetric cell is slightly higher than that of the pure Li symmetric cell, which may be due to the artificial SEI film formed by the AlF_3-treated lithium electrode. In addition, the EIS spectrum of a symmetric cell with pure Li before cycling has only one semicircle, and a single semicircle represents the R_{ct} between pure Li and the electrolyte. The higher R_{ct} of pure Li symmetric batteries can be attributed to the lower electrolyte wettability, resulting in slow Li^+ transport [30,31]. There is also an absence of protective layer to inhibit possible side reactions, resulting in electrolyte depletion and the unstable and fragile SEI formation, which ultimately increases the cell's impedance. In

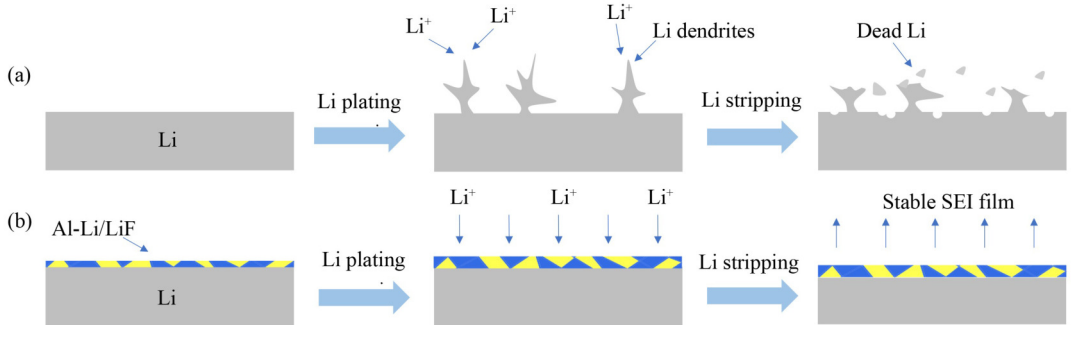

Fig. 1 Schematic illustration of (a) Li dendrites growth on bare Li and (b) smooth Li deposition on artificial SEI protected Li during the charge/discharge process.

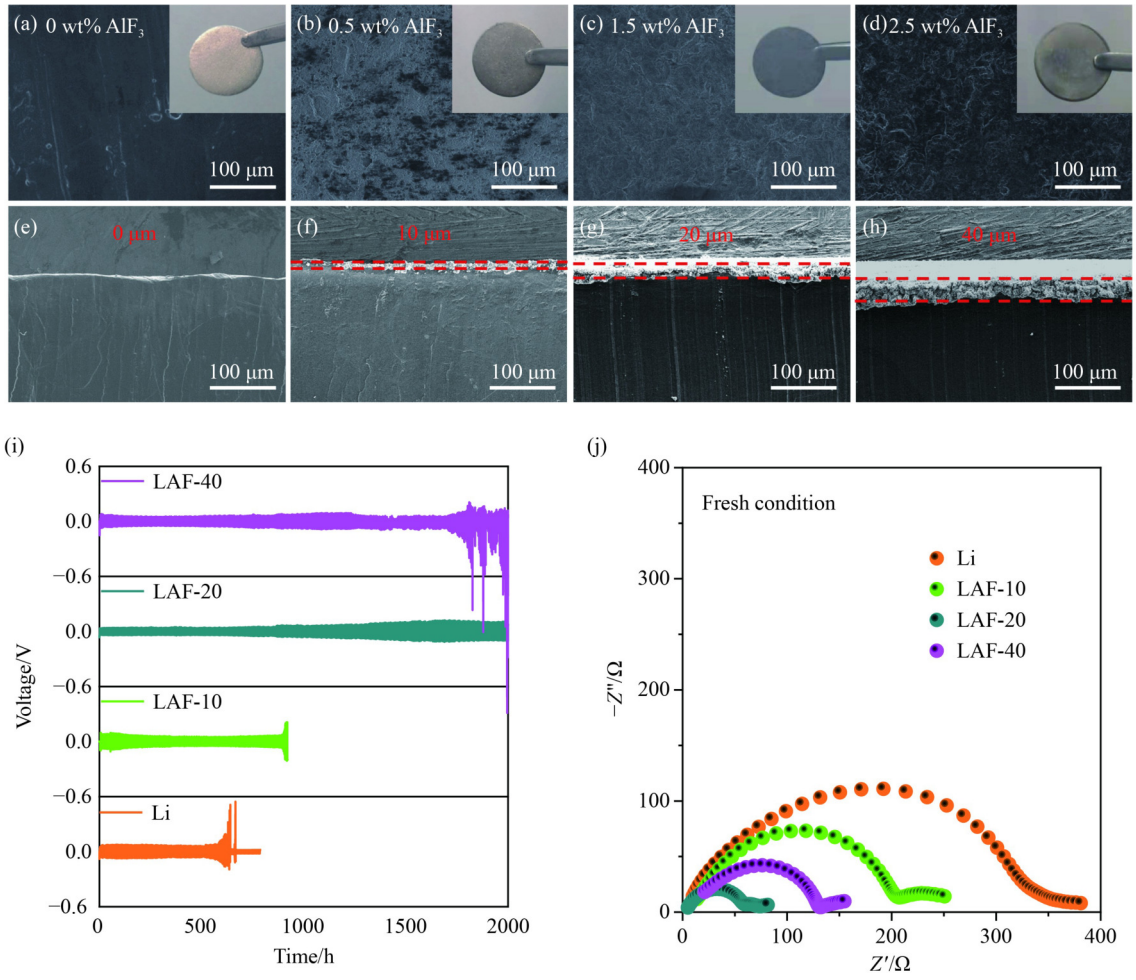

Fig. 2 Optimising the thickness of the SEI protective layer. (a–d) Top-view SEM images of Li with different weight percentage concentrations of AlF_3 (The inset picture is the corresponding photographic images). (e–h) The corresponding cross-sectional SEM images. (i) Time voltage curves of Li with different weight percentage concentrations of AlF_3. (j) Impedance at Li with different weight percentage concentrations of AlF_3.

contrast, LAF-10, LAF-20, LAF-40 symmetric cells present two semicircular circles, the first semicircle in the high-frequency range representing the interface resistance of the artificial SEI or the resistance R_{ct} through the artificial SEI, and the second semicircle in the low frequency range representing the R_{int} between the artificial SEI and the electrolyte. The R_{ct} of LAF-10, LAF-20 and LAF-40 symmetric batteries are low, which is attributed to the excellent electrolyte wetting property of artificial SEI, which effectively mitigates side reactions and then stabilizes the SEI layer. Furthermore, the LiF with higher surface energy in the SEI layer can provide, a lower Li^+ diffusion barrier. This allows sufficient Li^+ transport and lower R_{ct}. A symmetric cell based on the LAF-20 electrode has a minimum R_{ct} value of 58.36 Ω, which is related to the rapid transport of Li^+ with an optimal SEI thickness of 20 μm. As a result, 20 μm is the most appropriate modification layer thickness.

As illustrated in Fig. 3(a), a straightforward chemical pretreatment builds the Al-Li/LiF interfacial layer on the Li foil surface. Li^+ movement across the contact is accelerated by interface between the LiF and Al-Li alloy with superior ionic conductivity. Electrons are unable to pass through the composite interfacial layer due to the electron-insulating LiF. Subsequently, the combination of Al-Li and LiF permits Li metal to be deposited at the bottom, and their robust mechanical properties effectively suppress the formation of Li dendrites. Moreover, the composite interfacial layer can isolate the electrolyte from the fresh Li metal and its electrochemical stability guarantees the cycle life of the cell.

To observe the structure and morphology on the surface of LAF-20 electrode, SEM characteristization was conducted (Figs. 3(b–d)). From the corresponding energy dispersive spectroscopy (EDS) of the surface morphology, it can be seen that Al and F elements are evenly distributed in the surface layer. In addition, the composition of the artificial SEI layer is further analyzed by XRD and XPS. First, the phase transition of lithium is characterized by XRD and the composition of the artificial SEI layer is studied. An XRD pattern of the

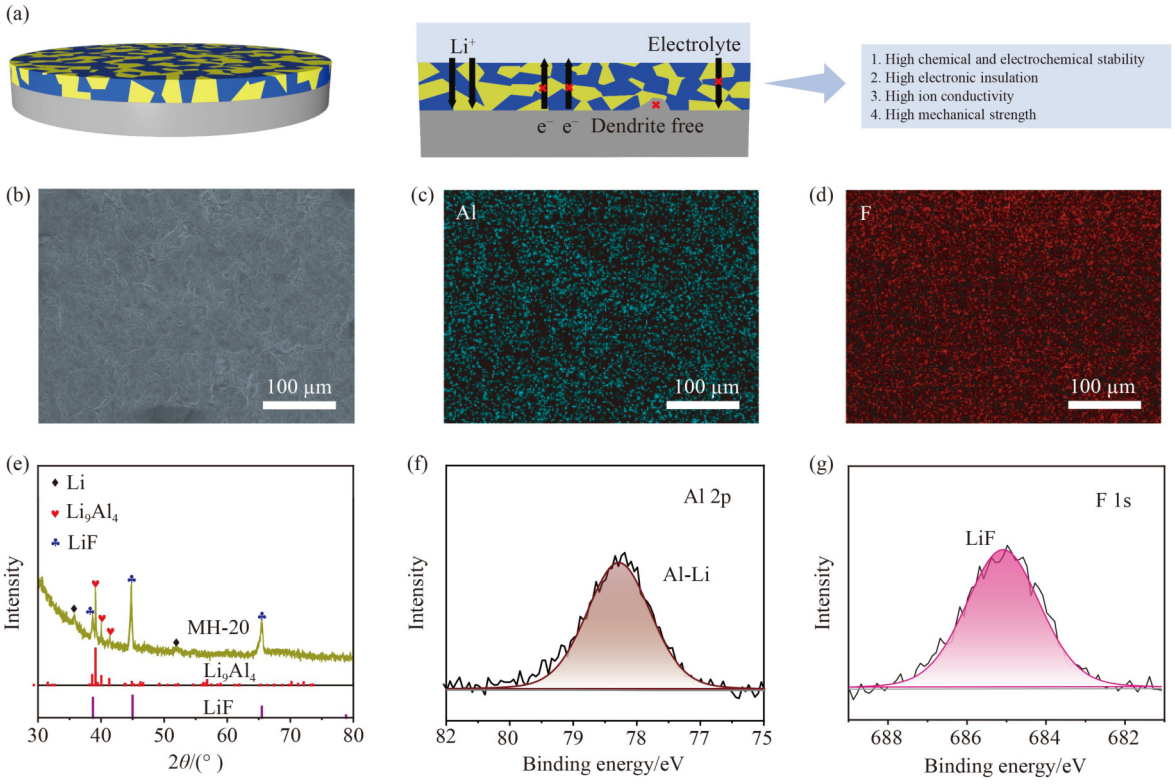

Fig. 3 Composition of the artificial SEI layer. (a) Schematic illustration of artificial SEI-protected Li and its function. (b) The SEM image of LAF-20 electrode and (c, d) the corresponding EDS. (e) XRD spectrum of LAF-20 electrode. XPS spectrum of LAF-20 electrode with (f) Al 2p and (g) F 1s.

LAF-20 electrode is shown in Fig. 3(e). The artificial SEI layer can form a beneficial aluminum-lithium alloy (Li_9Al_4) and LiF. The peaks at ca. 38.6°, 39.1° and 41.3° correspond to Li_9Al_4. The peaks of ca. 38.7°, 44.9°, and 65.4° correspond to LiF [32,33]. XPS is used to determine the chemical composition of SEI surface of LAF-20 electrode (Figs. 3(f) and 3(g)), corresponding to the peak of Al-Li alloy at 74.2 eV, the presence of the alloy helps to reduce the diffusion potential of Li^+ and improve the stability of the Li metal interface. A single F 1s peak at 685 eV corresponds to the presence of LiF, which regulates the uniform deposition/dissolution of lithium. By comparing the XPS spectra of pure Li and treated Li, it can be concluded that after AlF_3 treatment, LiF and Al-Li alloy are formed (Fig. S2, cf. ESM). In summary, the artificial SEI consists of a dense and homogeneous mixture of Al-Li and LiF.

The kinetics of interfacial Li^+ transport in the artificial SEI layer are further investigated. The tafel curve of pure Li and LAF-20 electrode are illustrated in Fig. 4(a). The results indicate that the exchange current density of LAF-20 electrode (0.937 $mA \cdot cm^{-2}$) is higher than that of pure Li electrode (0.112 $mA \cdot cm^{-2}$). This suggests that the modified electrode has high charge transfer kinetics and fast Li^+ transfer capabilities. In line with the electrochemical impedance results, the LAF-20 electrode demonstrates a lower R_{ct} compared to the pure Li electrode, and the hybrid artificial SEI can increase the speed of Li^+ transportation. The temperature-dependent electrochemical impedance spectroscopy is tested to investigate the activation energy of Li^+ diffusion in SEI at 303–353 K (Fig. S3, cf. ESM). By fitting the first semicircle of the symmetric cell with pure Li and LAF-20 electrodes using an equivalent circuit, the activation energy was determined, following Arrheniuz's law. As can be seen from Fig. 4(b), the activation energy of LAF-20 (4.69 $kJ \cdot mol^{-1}$) is lower than that of pure Li batteries (7.45 $kJ \cdot mol^{-1}$), indicating that artificial SEI can provide a fast Li ion transport channel. Figure S4 (cf. ESM) presents the EIS spectra of pure Li and LAF-20 electrode at various resting times. It is evident that the symmetric cell with LAF-20 electrode has better stability during the resting process compared to the pure Li electrode, further illustrates the good protective effect of the hybrid artificial SEI layer.

To gain a deeper understanding of the mechanism behind performance of the hybrid artificial SEI layer, AFM is used to test the Young's modulus of pure Li and LAF-20 electrodes (Fig. S5, cf. ESM). The results revealed that the average Young's modulus values are 1.1 and 53.3 GPa, respectively. The significantly higher Young's vmodulus of the LAF-20 electrode can be attributed to the combined contribution of all SEI components, namely LiF and Al-Li alloys. The strong ionic bond between lithium and fluorine results in a Young's modulus range of 50 to 140 GPa for LiF.

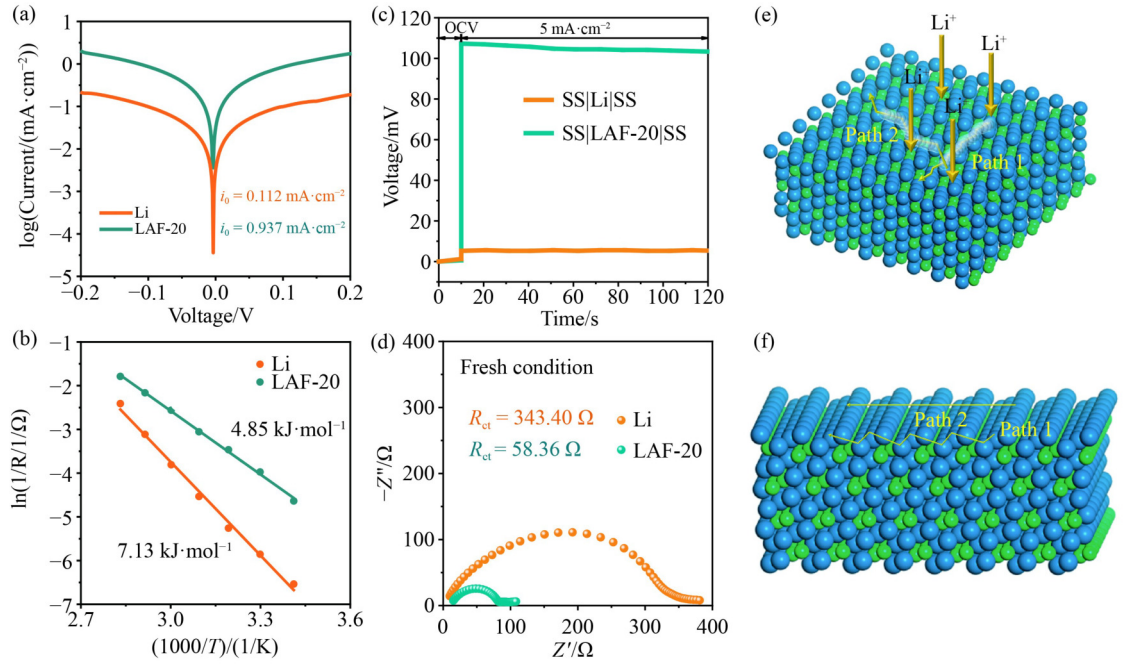

Fig. 4 The interfacial Li^+ transport kinetics. (a) Tafel profle of Li and LAF-20 electrode. (b) The activation energy for Li^+ diffusion through SEI of bare Li and LAF-20 electrode. (c) Voltage response of bare Li and LAF-20 electrode block cells. (d) Nyquist plot of bare Li and LAF-20 electrode symmetric cells. (e, f) DFT simulation results of the LAF-20 electrode.

Notably, the B1 crystal structure of LiF (analogous to the NaCl type) remains stable even at high pressures up to 100 GPa and high temperatures approaching its melting point [34−37]. Furthermore, lithium-based alloys exhibit significantly higher strength compared to bare Li metal [38,39]. Consequently, the artificial SEI possesses a high Young's modulus. Previous studies have highlighted the importance of a high modulus SEI in inhibiting dendrite growth [34,38]. In this context, the excellent mechanical strength of the artificial SEI acts as a barrier to dendrite growth, thereby protecting the LMA. Additionally, the contact angle measurements between the electrolyte and pure Li and LAF-20 electrodes revealed values of 35.46° and 19.38°, respectively (Fig. S6, cf. ESM). The high electrolyte affinity of the SEI layer enhances the contact between the electrolyte and anode, leading to a higher surface energy of the SEI layer. This, in turn, facilitates rapid diffusion and nucleation of Li^+, contributing to the overall performance of the hybrid artificial SEI layer.

To assess the resistivity of the hybrid artificial SEI layer, a direct current-voltage measurement was conducted utilizing the blocking electrode setup (Fig. 4(c)). Previous literature [40] has compared the current responses of SS||SS and SS||Li||SS configurations, revealing that the two curves are nearly identical. This indicates that the resistivity of pure Li metal is negligible, and any resistance observed is attributable to the experimental apparatus itself. In the present study, either pure Li or LAF-20 electrodes were sandwiched between two stainless steel blocking electrodes. The voltage response to a DC current density of 5.0 $mA·cm^{-2}$ was then recorded using the following formula:

$$\rho = \frac{R \times S}{L} = \frac{U \times S}{I \times L},$$

where L represents the total thickness of the artificial SEI layer, I is the applied current, S is the area of the Li metal electrode sheet, and U is the increase in the average voltage. The calculated resistivity of LAF-20 is 494.5 Ω·cm. The electronic resistivity of semiconductors typically ranges from 10^{-3} to 10^{9} Ω·cm. This indicates that the hybrid SEI protective layer of LAF-20 reduces electronic conductivity, and the resistance of the SEI facilitates preferential Li deposition beneath it. Consequently, even as the current density increases and the amount of Li deposition rises, the layer can still lower the local current density at the anode and ensure a more uniform distribution of Li ions. Due to the inherently low electronic conductivity of the SEI, the growth of Li dendrites is also inhibited. In this study, the interface resistance of the LAF-20 symmetric cell is 58.36 Ω, compared to 343.40 Ω for pure Li, which reflects the diffusion of Li ions. The SEI formed *in situ* on pure Li typically has a thickness of less than 100 nm, whereas the artificial SEI has a thickness of 20 μm. Therefore, it can be inferred that if the ionic conductivity remains constant, the ionic conductivity of the hybrid SEI is hundreds of times that of pure Li. Moreover, the lower interface resistance of the thicker artificial SEI confirms its higher ionic conductivity (Fig. 4(d)). In summary, the artificial SEI exhibits high ionic conductivity and low electronic conductivity, enabling it to not only prevent Li ion deposition on the surface layer but also promote rapid ion

transport.

Furthermore, the influence of alloys at the interface has been investigated. Density functional theory (DFT) was employed to ascertain the surface diffusion barrier of the Li_9Al_4 (100) alloy. The surface diffusion barriers for the Li_9Al_4 (100) alloy are merely 0.013 and 0.189 eV, with surface adsorption energies of 0.24, 0.77, and 0.76 eV, respectively. These values are significantly lower than those for Li (100), which has a surface diffusion barrier of 0.305 eV and an adsorption energy of 1.792 eV (Figs. 4(e) and 4(f)). The rapid conduction of Li^+ ions in the Li_9Al_4 alloy ensures that lithium can efficiently diffuse deeper into the SEI during deposition, leading to a more uniform distribution. However, in the case of a pure Li electrode, the combination of a high diffusion barrier and strong adsorption capacity causes Li metal to preferentially grow on the surface, forming one-dimensional structures and ultimately resulting in Li dendrites. Therefore, the Al-Li alloy within the hybrid artificial SEI effectively facilitates the rapid conduction of Li^+ ions and promotes the deposition of Li^+ ions at the bottom layer.

The interfacial stability of pure Li and LAF-20 electrodes has been further investigated. Figures 5(a) and 5(c) present the symmetric battery profiles for pure Li and LAF-20 electrodes at current densities of 0.5 and 1 $mA \cdot cm^{-2}$, respectively. Pure Li cells exhibit a cycle life of approximately 600 and 300 h at 0.5 and 1 $mA \cdot cm^{-2}$ current densities, respectively, with a continuous rise in overpotential leading to a shortened cycle life. In contrast, symmetric cells incorporating LAF-20 electrodes display a stable voltage curve over extended cycling periods. The deposition/dissolution time for LAF-20 symmetric batteries exceeds 2300 and 700 h at 0.5 and 1 $mA \cdot cm^{-2}$ current densities, respectively. In the case of pure Li,

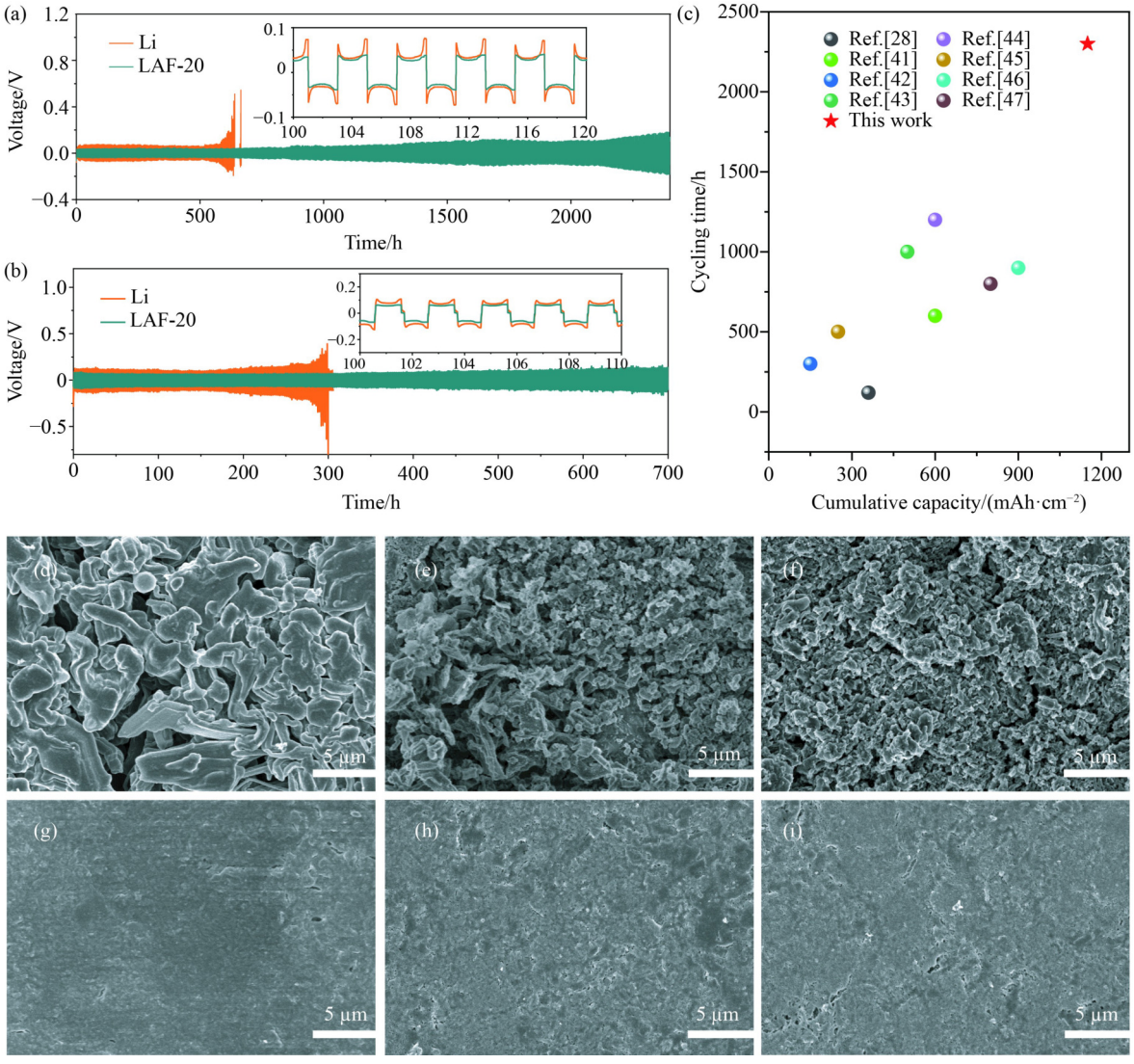

Fig. 5 The electrochemical performance of the LAF-20 electrodes. (a) Plating/stripping voltage profile of bare Li and LAF-20 electrode symmetric cells at 0.5 $mA \cdot cm^{-2}$ (inset: the partial amplified curve of (a)). (b) Plating/stripping voltage profile of bare Li and LAF-20 electrode at 1 $mA \cdot cm^{-2}$ (inset: the partial amplified curve of (b)). (c) The comparison of cycling time and cumulative capacity of this work with previous reports. The SEM of (d–f) bare Li and (g–i) LAF-20 at 1st, 10th, and 100th plating, respectively.

uneven Li deposition during cycling results in the formation of Li dendrites and a fragile, unstable SEI due to the reaction between lithium and the electrolyte. This leads to electrolyte depletion and a continuous increase in overpotential, ultimately causing premature cell shorting. Conversely, the hybrid SEI formed by AlF_3 treatment effectively suppresses side reactions between lithium and the electrolyte while promoting uniform Li deposition. As illustrated in Figs. 5(b) and 5(d), symmetric batteries with LAF-20 electrodes exhibit lower nucleation overpotential. The time-voltage curve demonstrates similar results at higher constant current densities (Figs. S7 and S8, cf. ESM).

When compared to previous work reported in the literature (Table S1, cf. ESM), the present study exhibits superior cyclic performance [28, 41−47]. Additional testing on the effect of LAF-20 on CE, as shown in Fig. S9 (cf. ESM), demonstrates improved CE for the reversibility of lithium deposition. Furthermore, the impedance spectra of the symmetric cell after different cycles further illustrate that the artificial interface coating can effectively stabilize the LMA (Fig. S10, cf. ESM). The deposition morphology of pure Li and LAF-20 electrodes after cycling has been examined using SEM. Figures 5(e–j) present the SEM images of both pure Li and LAF-20 electrodes following deposition at the 1st, 10th, and 100th cycles, conducted at a current density of 0.5 $mA \cdot cm^{-2}$ with a capacity of 1 $mAh \cdot cm^{-2}$. The pure Li electrodes (depicted in Figs. 5(e–g)) exhibit considerable surface roughness and random outward projections of fibrous Li dendrites. Conversely, the surface of the LAF-20 electrodes (shown in Figs. 5(h–j)) is notably flat and smooth, devoid of any significant dendritic or mossy lithium formations. This can be attributed to the dense and uniform artificial SEI layer, which serves as a physical barrier to prevent the penetration of the organic electrolyte and the ensuing corrosion of the underlying lithium electrode. Furthermore, the insulating LiF present in the SEI component is not favorable for lithium nucleation but facilitates Li ion diffusion. It stores lithium by depositing beneath the lithium electrode, thereby promoting uniform and smooth Li deposition. Cross-sectional SEM images of the bare Li and LAF-20 anodes post-cycling corroborate that the artificial interface layer effectively curtails dendrite growth and stabilizes Li metal (Fig. S11, cf. ESM). The surface chemical composition of both bare Li and LAF-20 after 20 cycles was further ascertained using XPS. By examining the C 1s, O 1s, and F 1s spectra (Figs. S12(a) and S12(b)), it can be inferred that the SEI formed on LAF-20 exhibits a reduced content of side reaction organic peaks (CO_3^{2-}) and an elevated content of inorganic components such as LiF and Li_2O. This suggests that the LAF-20 interfacial layer aids in suppressing interface side reactions. Figure S12(c) presents XPS depth profiles of LAF-20 after 20 cycles, with an etching depth of 100 nm, where LiF and Li-Al alloy are still clearly discernible. LAF-20 appears to exist stably on the Li metal surface, mitigating electrolyte consumption and significantly enhancing Li^+ transport. Consequently, it can be affirmed that the upper surface region of the SEI predominantly comprises Li-Al alloy and Li-based compounds (LiF, LiOR, Li_2CO_3, and Li_2O). In the inner region, Li-Al alloy and LiF constitute the major components (Fig. S13, cf. ESM).

To assess the potential applicability and feasibility of LAF-20 electrodes in practical cells, full LMBs were assembled using LFP and NCM811 as cathodes, respectively. Figure 6(a) illustrates the cycling performance of full cells employing pure Li and LAF-20 as anodes, with LFP as the cathode, within a voltage range of 2.5–3.8 V at 1 C. The LAF-20||LFP full cell exhibited remarkable cycle stability, delivering a discharge capacity of 114.3 $mAh \cdot g^{-1}$ after 300 cycles and a capacity retention rate of 75.5%. In comparison, the Li||LFP full cell provided a discharge capacity of 85.8 $mAh \cdot g^{-1}$ after 300 cycles, with a capacity retention rate of 60%. The inferior CE observed in the pure Li||LFP full cell can be attributed to side reactions leading to the formation of an unstable and brittle SEI. As depicted in Fig. 6(b), the LAF-20||LFP full cell demonstrates superior rate performance, aligning with the results from symmetric cell tests and impedance measurements. Figure 6(c) reveals that the polarization voltage of the LAF-20||LFP full cell is lower than that of the pure Li||LFP full cell during the first cycle. When comparing the voltage curves of the 1st and 100th cycles, it becomes evident that the capacity decay rate of the LAF-20||LFP full cell is lower than that of the Li||LFP full cell, owing to the slower interfacial dynamics between pure Li and the electrolyte.

Figure S14 (cf. ESM) presents the EIS spectrum of a full cell with an LFP cathode and either pure Li or LAF-20 as the anode. The significant reduction in R_{ct} observed for the LAF-20 anode indicates an enhancement in charge transfer kinetics. Figure S15 (cf. ESM) showcases SEM images of the full cell electrodes after 100 cycles, comparing pure Li and LAF-20. The LAF-20 electrode surface remains highly smooth and dense, closely resembling its initial state. In contrast, the pure Li electrode surface appears quite rough and exhibits a porous morphology. This further demonstrates that the LAF-20 electrode provides an excellent protective effect for Li metal.

Figure 6(d) illustrates the long-term cycle performance of a full cell, employing either pure Li or LAF-20 as the anode and NCM811 as the cathode, at 1 C within a voltage range of 2.8–4.3 V. The full cell test was initiated at 0.1 C for three cycles. The LAF-20||NCM811 full cell exhibits outstanding cycle stability, maintaining a discharge capacity of 137 $mAh \cdot g^{-1}$ after 300 cycles. Conversely, the Li||NCM811 full cell experiences noticeable capacity attenuation after just 150 cycles. The LAF-20||NCM811 full cell has demonstrated remarkable cycle stability over an extended period. Furthermore, the

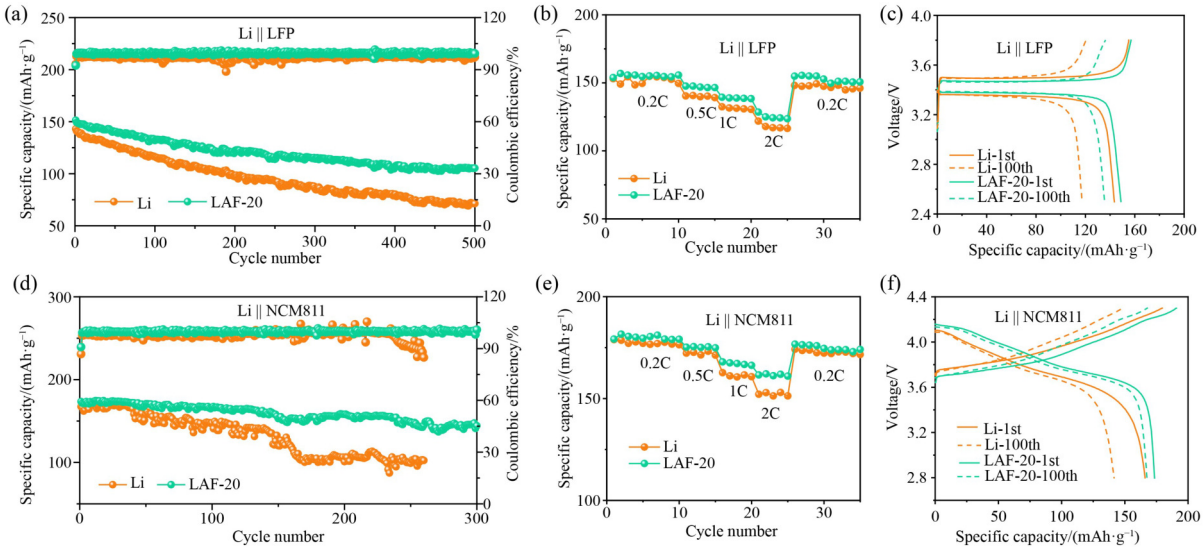

Fig. 6 The electrochemical performance of the full cells. (a) Long-term cycling performance of LFP coupled with bare Li and LAF-20 anode full cells at a current density of 1 C. (b) Rate capability comparison of LFP coupled with bare Li and LAF-20 anode full cells. (c) The first cycle and 100th cycle charge/discharge curve of Li||LFP full cells using pure Li and LAF-20 anode a current density of 1 C. (d) Long-term cycling performance of full cells at a current density of 1 C. (e) Rate capability comparison of NCM811 coupled with bare Li and LAF-20 anode full cells. (f) The first cycle and 100th cycle charge/discharge curve of Li||NCM811 full cells using pure Li and LAF-20 anode at 1 C.

LAF-20||NCM811 full cell offers superior rate performance, as depicted in Fig. 6(e). As evident from Fig. 6(f), the polarization voltage of the LAF-20||NCM811 full cell is lower than that of the pure Li||NCM811 full cell during the first cycle. This reduced polarization voltage suggests that Li^+ ions can traverse the hybrid SEI layer rapidly, thanks to the presence of the hybrid SEI. The rapid increase in polarization voltage observed in pure Li cells with cycling is primarily attributed to the unstable SEI. When comparing the voltage curves of the 1st and 100th cycles, it becomes apparent that the capacity decay rate of the LAF-20||NCM811 full cell is lower than that of the Li||NCM811 full cell, due to the slower interfacial dynamics between pure Li and the electrolyte.

Figure S16 (cf. ESM) presents the EIS spectrum of a full cell with NCM811 as the cathode and either pure Li or LAF-20 as the anode. The substantial reduction in R_{ct} observed for the LAF-20 anode indicates an improvement in charge transfer dynamics. The anode is protected by a hybrid artificial SEI comprising LiF and Al-Li alloys, which facilitates adequate diffusion of Li ions while inhibiting detrimental side reactions. Figure S17 (cf. ESM) showcases SEM images of the pure Li and LAF-20 electrodes after 100 cycles of the cell. The surface of the LAF-20 electrode appears notably flat, whereas the surface of the pure Li electrode is rough and porous.

4 Conclusions

An artificial SEI, enriched with LiF and Al-Li alloys, is formed by modifying the LMA with AlF_3. This hybrid artificial SEI exhibits high ion conductivity, low electron conductivity, and excellent mechanical properties. It effectively inhibits side reactions between the lithium anode and electrolyte, as well as the growth of lithium dendrites, while allowing for rapid lithium ion transport and deposition beneath it. Li||Li symmetric batteries can stably deposit and dissolve lithium for an extended period of time (~2300 h) at a low overpotential. Full cells incorporating this modified anode demonstrate enhanced cycle stability and capacity retention. Specifically, the LAF-20||LFP full cell exhibits a discharge capacity of 114.3 $mAh \cdot g^{-1}$ after 300 cycles, with a capacity retention rate of 75.5%. Similarly, the LAF-20||NCM811 full cell displays a discharge capacity of 137 $mAh \cdot g^{-1}$ after 300 cycles. This approach, based on metal fluoride-induced interfacial phase stabilization of the LMA, offers a novel strategy for the development of high-energy density energy storage devices.

Acknowledgements This work is supported by the National Natural Science Foundation of China (Grant No. 22278308); Beijing-Tianjin-Hebei Basic Research Cooperation Special Project (Grant No. B2024209048); the Natural Science Foundation of Tianjin, China (Grant No. 24JCZXJC00250); the Natural Science Foundation of Henan Province (Grant No. 242300421431) and the China Postdoctoral Science Foundation (Grant No. 2022M712863).

Electronic Supplementary Material Supplementary material is available in the online version of this article at https://doi.org/10.1007/s11705-025-2539-0 and is accessible for authorized users.

Competing interests The authors declare that they have no competing interests.

References

1. Wang Z, Xia J, Ji X, Liu Y, Zhang J, He X, Zhang W, Wan H, Wang C. Lithium anode interlayer design for all-solid-state lithium-metal batteries. Nature Energy, 2024, 9(3): 251–262
2. Jia J, Guo B, Gao H, Zhao Y, Li G, Wang A, Liu C. Stabilizing sodium metal anodes by functional polymers. Materials Today. Energy, 2024, 45: 101664
3. Ye S, Chen X, Zhang R, Jiang Y, Huang F, Huang H, Yao Y, Jiao S, Chen X, Zhang Q, et al. Revisiting the role of physical confinement and chemical regulation of 3D hosts for dendrite-free Li metal anode. Nano-Micro Letters, 2022, 14(1): 187
4. Li G, Guan X, Wang A, Wang C, Luo J. Cations and anions regulation through zwitterionic gel electrolytes for stable lithium metal anodes. Energy Storage Materials, 2020, 24: 574–578
5. Xia Q, Yuan S, Zhang Q, Huang C, Liu J, Jin H. Designing the interface layer of solid electrolytes for all-solid-state lithium batteries. Advanced Science, 2024, 11(29): 2401453
6. Wang A, Nie Y, Zhao Y, Xu D, Zhang L, Zhao Z, Ren L, Zhou S, Liu X, Luo J. Functional copolymer derived self-adapting LiF-rich interphase toward deep cycling lithium metal batteries. Advanced Functional Materials, 2024, 34(29): 2401462
7. Xu D, Zhou N, Wang A, Xu Y, Liu X, Tang S, Luo J. Mechano-electrochemically promoting lithium atom diffusion and relieving accumulative stress for deep-cycling lithium metal anodes. Advanced Materials, 2023, 35(35): 2302872
8. Zhang C, Liu S, Li G, Zhang C, Liu X, Luo J. Incorporating ionic paths into 3D conducting scaffolds for high volumetric and areal capacity, high rate lithium-metal anodes. Advanced Materials, 2018, 30(33): 1801328
9. Wu L, Lv H, Zhang R, Ding P, Tang M, Liu S, Wang L, Liu F, Guo X, Yu H. Ferroelectric $BaTiO_3$ regulating the local electric field for interfacial stability in solid-state lithium metal batteries. ACS Nano, 2024, 18(7): 5498–5509
10. Mao M, Ji X, Wang Q, Lin Z, Li M, Liu T, Wang C, Hu Y S, Li H, Huang X, et al. Anion-enrichment interface enables high-voltage anode-free lithium metal batteries. Nature Communications, 2023, 14(1): 1082
11. Liu P, Shen S, Qiu Z, Yang T, Liu Y, Su H, Zhang Y, Li J, Cao F, Zhong Y, et al. Plasma coupled electrolyte additive strategy for construction of high-performance solid electrolyte interphase on Li metal anodes. Advanced Materials, 2024, 36(30): 2312812
12. Zhuang H, Xiao H, Zhang T, Zhang F, Han P, Xu M, Dai W, Jiao J, Jiang L, Gao Q. LiF-rich alloy-doped SEI enabling ultra-stable and high-rate Li metal anode. Angewandte Chemie International Edition, 2024, 63(33): e202407315
13. Lu W, Zhao A, Chen Q, Liu S, Yu M, Wang Z, Gao Z, Zhao X, Sun G, Feng M. Constructing lithiophilic sites-rich artificial solid electrolyte interphase to enable dendrite-free and corrosion-free lithium-sulfur batteries. Green Energy & Environment, 2024, 9(12): 1891–1900
14. Xie S, Yu S, Hou Y, Dong F, Zhang X, Zheng H, Xie H, Wang Z, Liu Y. Ga-polymer dual interfacial layer modified Li metal for high-energy Li metal batteries. Journal of Energy Storage, 2024, 91: 112056
15. Tan P, Wang Y, Sun X, Zhou Y, Dong H, Han Y, Li D. Self-limiting lithium deposition enabled by synergistic surface chemical and structural engineering of Li metal anodes. Journal of Alloys and Compounds, 2024, 996: 174867
16. Shi M, Zhang J, Tang G, Wang B, Wang S, Ren X, Li G, Chen W, Liu C, Shen C. Polyzwitterionic cross-linked double network hydrogel electrolyte enabling high-stable Zn anode. Nano Research, 2024, 17(6): 5278–5287
17. Zhang Y, Guo Y, Yong K, Wang Q, Yao M, Zhang Y, Wu H. A large-capacity, superhigh-rate integrated lithium metal anode with top-down composition gradient enabled by polyantimonic acid. Energy & Environmental Science, 2024, 17(16): 5819–5832
18. Cao J, Shi Y, Gao A, Du G, Dilxat M, Zhang Y, Cai M, Qian G, Lu X, Xie F, et al. Hierarchical Li electrochemistry using alloy-type anode for high-energy-density Li metal batteries. Nature Communications, 2024, 15(1): 1354
19. Pathak R, Chen K, Gurung A, Reza K M, Bahrami B, Pokharel J, Baniya A, He W, Wu F, Zhou Y, et al. Fluorinated hybrid solid-electrolyte-interphase for dendrite-free lithium deposition. Nature Communications, 2020, 11(1): 93
20. Tan Y, Sun Z, Liu Y, Yan H, Wang C, Fan J, Zheng M, Dong Q. Constructing an ion-wall to achieve excellent lithium anodes in Li-O_2 batteries with high DN electrolytes. Advanced Energy Materials, 2024, 14(17): 2304153
21. Long K, Huang S, Wang H, Wang A, Chen Y, Liu Z, Zhang Y, Wu Z, Wang W, Chen L. Green mechanochemical Li foil surface reconstruction toward long-life Li-metal pouch cells. Energy & Environmental Science, 2024, 17(1): 260–273
22. Zhang C H, Guo Y J, Tan S J, Wang Y H, Guo J C, Tian Y F, Zhang X S, Liu B Z, Xin S, Zhang J, et al. An ultralight, pulverization-free integrated anode toward lithium-less lithium metal batteries. Science Advances, 2024, 10(13): eadl4842
23. Zhang Y, Yao M, Wang T, Wu H, Zhang Y. A 3D hierarchical host with gradient-distributed dielectric properties toward dendrite-free lithium metal anode. Angewandte Chemie International Edition, 2024, 63(22): e202403399
24. Zhai P, Liu L, Gu X, Wang T, Gong Y. Interface engineering for lithium metal anodes in liquid electrolyte. Advanced Energy Materials, 2020, 10(34): 2001257
25. Lim H, Jun S, Song Y B, Baeck K H, Bae H, Lee G, Kim J, Jung Y S. Rationally designed conversion-type lithium metal protective layer for all-solid-state lithium metal batteries. Advanced Energy Materials, 2024, 14(12): 2303762
26. Pan J, Cheng Y T, Qi Y. General method to predict voltage-dependent ionic conduction in a solid electrolyte coating on electrodes. Physical Review B: Condensed Matter and Materials Physics, 2015, 91(13): 134116
27. Yuan Y, Wu F, Bai Y, Li Y, Chen G, Wang Z, Wu C. Regulating Li deposition by constructing LiF-rich host for dendrite-free lithium metal anode. Energy Storage Materials, 2019, 16: 411–418
28. Zhao J, Liao L, Shi F, Lei T, Chen G, Pei A, Sun J, Yan K, Zhou G, Xie J, et al. Surface fluorination of reactive battery anode materials for enhanced stability. Journal of the American Chemical Society, 2017, 139(33): 11550–11558
29. Tu Z, Choudhury S, Zachman M J, Wei S, Zhang K, Kourkoutis L F, Archer L A. Fast ion transport at solid-solid interfaces in

hybrid battery anodes. Nature Energy, 2018, 3(4): 310–316

30. Pang M, Jiang Z, Luo C, Yao Z, Fu T, Pan T, Guo Q, Li Y, Xiong S, Zheng C, et al. A surface chemistry-regulated gradient multi-component solid electrolyte interphase for a 460 $Wh \cdot kg^{-1}$ lithium metal pouch cell. Energy & Environmental Science, 2024, 17(20): 7699–7711
31. Tan L, Chen P, Chen Q Y, Huang X, Zou K Y, Nie Y M, Li L J A. Li_3Bi/LiF interfacial layer enabling highly stable lithium metal anode. Rare Metals, 2023, 42(12): 4081–4090
32. Wang L, Fu S, Zhao T, Qian J, Chen N, Li L, Wu F, Chen R. *In situ* formation of a LiF and Li-Al alloy anode protected layer on a Li metal anode with enhanced cycle life. Journal of Materials Chemistry A: Materials for Energy and Sustainability, 2020, 8(3): 1247–1253
33. Wang H, Lin D, Liu Y, Li Y, Cui Y. Ultrahigh-current density anodes with interconnected Li metal reservoir through overlithiation of mesoporous AlF_3 framework. Science Advances, 2017, 3(9): e1701301
34. Ma L, Kim M S, Archer L A. Stable artificial solid electrolyte interphases for lithium batteries. Chemistry of Materials, 2017, 29(10): 4181–4189
35. Zhang X, Wang S, Xue C, Xin C, Lin Y, Shen Y, Li L, Nan C W. Self-suppression of lithium dendrite in all-solid-state lithium metal batteries with poly(vinylidene difluoride)-based solid electrolytes. Advanced Materials, 2019, 31(11): 1806082
36. Smirnov N A. Ab initio calculations of the thermodynamic properties of LiF crystal. Physical Review B: Condensed Matter and Materials Physics, 2011, 83(1): 014109
37. Ryu J, Kang J, Kim H, Lee J H, Lee H, Park S. Electrolyte-mediated nanograin intermetallic formation enables superionic conduction and electrode stability in rechargeable batteries. Energy Storage Materials, 2020, 33: 164–172
38. Lu Z, Li W, Long Y, Liang J, Liang Q, Wu S, Tao Y, Weng Z, Lv W, Yang Q H. Constructing a high-strength solid electrolyte layer by in vivo alloying with aluminum for an ultrahigh-rate lithium metal anode. Advanced Functional Materials, 2020, 30(7): 1907343
39. Lee H, Lee D J, Kim Y J, Park J K, Kim H T. A simple composite protective layer coating that enhances the cycling stability of lithium metal batteries. Journal of Power Sources, 2015, 284: 103–108
40. Liang X, Pang Q, Kochetkov I R, Sempere M S, Huang H, Sun X, Nazar L F. A facile surface chemistry route to a stabilized lithium metal anode. Nature Energy, 2017, 2(9): 17119
41. Lu K, Gao S, Dick R J, Sattar Z, Cheng Y. A fast and stable Li metal anode incorporating an Mo_6S_8 artificial interphase with super Li-ion conductivity. Journal of Materials Chemistry A: Materials for Energy and Sustainability, 2019, 7(11): 6038–6044
42. Gao Y, Zhao Y, Li Y C, Huang Q, Mallouk T E, Wang D. Interfacial chemistry regulation via a skin-grafting strategy enables high-performance lithium-metal batteries. Journal of the American Chemical Society, 2017, 139(43): 15288–15291
43. Peng Z, Song J, Huai L, Jia H, Xiao B, Zou L, Zhu G, Martinez A, Roy S, Murugesan V, et al. Enhanced stability of Li metal anodes by synergetic control of nucleation and the solid electrolyte interphase. Advanced Energy Materials, 2019, 9(42): 1901764
44. Wang L, Zhang L, Wang Q, Li W, Wu B, Jia W, Wang Y, Li J, Li H. Long lifespan lithium metal anodes enabled by Al_2O_3 sputter coating. Energy Storage Materials, 2018, 10: 16–23
45. Naren T, Kuang G C, Jiang R, Qing P, Yang H, Lin J, Chen Y, Wei W, Ji X, Chen L. Reactive polymer as artificial solid electrolyte interface for stable lithium metal batteries. Angewandte Chemie International Edition, 2023, 62(26): e202305287
46. Fang S, Wu F, Zhao S, Zarrabeitia M, Kim G T, Kim J K, Zhou N, Passerini S. Adaptive multi-site gradient adsorption of siloxane-based protective layers enable high performance lithium-metal batteries. Advanced Energy Materials, 2023, 13(46): 2302577
47. Li C, Liang Z, Li Z, Cao D, Zuo D, Chang J, Wang J, Deng Y, Liu K, Kong X, et al. Self-assembly monolayer inspired stable artificial solid electrolyte interphase design for next-generation lithium metal batteries. Nano Letters, 2023, 23(9): 4014–4022